ACS APPLIED MATERIALS & INTERFACES

Research Article

Cite This: ACS Appl. Mater. Interfaces 2019, 11, 31851−31859

www.acsami.org

Self-Organized Back Surface Field to Improve the Performance of $Cu_2ZnSn(S,Se)_4$ Solar Cells by Applying P-Type $MoSe_2$:Nb to the Back Electrode Interface

Yanping Song,[†,‡] Bin Yao,*[,†,‡] Yongfeng Li,*[,†,‡] Zhanhui Ding,[†,‡] Huanhuan Sun,[†,‡] Zhenzhong Zhang,[§] Ligong Zhang,[§] and Haifeng Zhao[§]

[†]State Key Lab of Superhard Materials and [‡]Key Laboratory of Physics and Technology for Advanced Batteries (Ministry of Education), College of Physics, Jilin University, Changchun 130012, China

[§]State Key Laboratory of Luminescence and Applications, Changchun Institute of Optics, Fine Mechanics and Physics, Chinese Academy of Sciences, No. 3888 Dongnanhu Road, Changchun 130033, China

Supporting Information

ABSTRACT: $Cu_2ZnSn(S,Se)_4$ (CZTSSe) thin-film solar cells have been encountering a bottleneck period since the champion power conversion efficiency (PCE) of 12.7% was achieved by Kim et al. in 2014. One of the critical factors that impede its further development is the relatively low open-circuit voltage (V_{OC}) caused by serious interface carrier recombination. In this regard, back surface field (BSF) employment is a feasible strategy to address the V_{OC} issue of CZTSSe solar cells to some extent. Here, we demonstrated a self-organized BSF introduced by prompting interfacial $MoSe_2$ layer transition from inherent n-type to desirable p-type with Nb doping (p-$MoSe_2$:Nb). The BSF application can significantly reduce the carrier recombination at the back electrode interface (BEI) and lower down the back contact barrier height. The PCE of the corresponding cell was improved from 4.72 to 7.15% because of the enhancement of V_{OC} and fill factor, primarily stemming from the doubling aspects of increased shunt resistance (R_{Sh}), decreased series resistance (R_S), and alleviative recombination velocity of the BEI induced by the BSF. Our results suggest that introducing a BSF fulfilled with p-$MoSe_2$:Nb is a facile and promising route to improve the performance of CZTSSe thin-film solar cells.

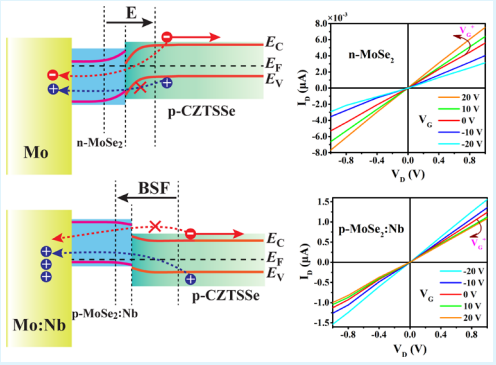

KEYWORDS: *$Cu_2ZnSn(S,Se)_4$, solar cells, back surface field, p-$MoSe_2$:Nb, carrier recombination, shunt resistance, series resistance*

INTRODUCTION

With the increase of global energy demand in the 21st century, renewable energy has attracted much attention given its advantages of less pollution and renewability. Among the renewable energy sources, photovoltaic (PV) solar energy is considered to be the most promising and potentially widely applicable one. Kesterite $Cu_2ZnSn(S_{1-x}Se_x)_4$ (CZTSSe) is one of the desirable candidates for high-efficiency thin-film solar cells owing to its natural abundance, suitable and easily tunable band gap (E_g) of 1.0−1.5 eV, and high optical absorption coefficient of over 10^4 cm^{-1}.[1−6] Over the past decades, PV devices based on CZTSSe thin films have been developed rapidly and the power conversion efficiency (PCE) was boosted from 5% in 2004 up to 12.7% in 2014.[1,3] However, as far as the record PCE is concerned, no conspicuous progress has been achieved since 2014. There still has been a large performance gap between CZTSSe and the counterpart $Cu(In,Ga)Se_2$ (CIGS) solar cells, which is primarily because of its low open-circuit voltage (V_{OC}) or high V_{OC} deficit (E_g/q-V_{OC}). One of the principal elements limiting the V_{OC} improvement is the carrier recombination at the back electrode interface (BEI) between absorber and inherent n-type interfacial $MoSe_2$ layer generated through an indispensable selenization process.[7] Figure 1 illustrates the schematic device structure of a typical CZTSSe solar cell with an interfacial $MoSe_2$ layer. The band diagram at BEI between n-$MoSe_2$ and p-CZTSSe is shown at the bottom-left of Figure 1. The n-type interfacial layer causes two unfavorable functions by forming an n-$MoSe_2$/p-CZTSSe interface. One is to drive electrons into BEI to increase recombination, and the other is to form a barrier to hinder holes into the back electrode, being detrimental for device performance.

To reduce the recombination at BEI, introducing a back surface field (BSF) into BEI is a facile and effective method.[8,9] Also, BSF lowers down the back contact barrier height.[8,9] However, to the best of our knowledge, surprisingly little attention has been devoted to focusing on the BSF application in CZTSSe solar cells so far. Omrani et al.[10] predicted that the

Received: May 22, 2019
Accepted: July 17, 2019
Published: July 17, 2019

DOI: 10.1021/acsami.9b08946
ACS Appl. Mater. Interfaces 2019, 11, 31851−31859

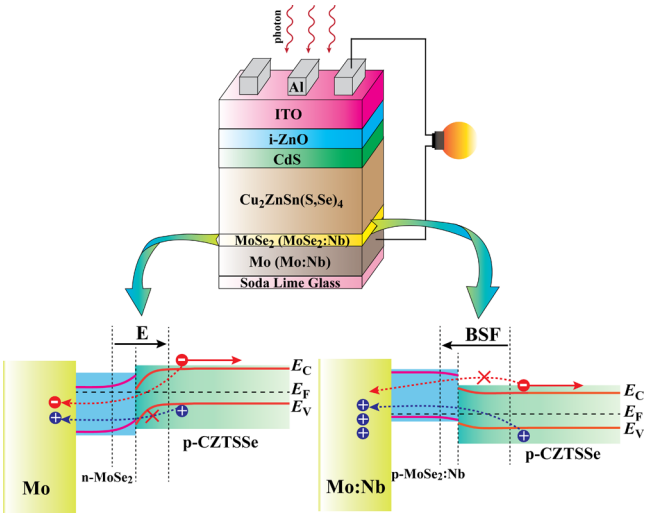

Figure 1. Schematic device structure of a typical CZTSSe solar cell (top) and the corresponding band diagrams at the BEI without (bottom-left) and with BSF (bottom-right), respectively.

PCE of CZTSSe devices increases from 12.3 to 17.25% using SnS as the BSF layer by solar cell capacitance simulator (SCAPS) software. Khattak et al.[11] also performed a numerical modeling study on PCE of CZTS solar cells without and with a CZTSe BSF layer via SCAPS, indicating that the PCE of CZTS solar cells with BSF was boosted from 6.42 to 12.92%. No experimental investigations have been undertaken for the device performance improvement of CZTSSe solar cells by introducing BSF.

A beneficial effect of BSF is to drive the photo-induced holes into back electrode. However, the barrier at the n-$MoSe_2$/p-CZTSSe interface blocks the hole transportation to some degree. The lowering of the barrier height can be expected if the conduction type of the interfacial $MoSe_2$ layer is transformed from n- to p-type, facilitating the hole transportation from the absorber to the back electrode. A band diagram at the BEI of CZTSSe solar cells with BSF is shown at the bottom-right of Figure 1. Regarding the transition of conduction type, elemental doping is employed commonly in transition-metal dichalcogenides (TMdCs).[12,13] It has been reported that Nb (five valance electrons) could be adopted as a substitutional p-type dopant to replace Mo with six valance electrons, where Nb exhibits no miscibility gap in MoNb alloys.[13,14] Therefore, in this work, Nb was doped into the interfacial $MoSe_2$ layer of CZTSSe solar cells to form a p-$MoSe_2$:Nb/p-CZTSSe interface (bottom-right of Figure 1); then, self-organized BSF generated through indispensable selenization process, leading to the contrary functions compared to the aforementioned case involving n-$MoSe_2$. Remarkably, BSF in our work is totally different from the other case that was realized externally (such as SnS,[10] CZTSe,[11] etc.) with more complicated processes before absorber preparation. By introducing BSF, the PCE of CZTSSe solar cell has been improved considerably from 4.72 to 7.15% because of the enhancement of V_{OC}, as well as fill factor (FF) and short-circuit current density (J_{SC}). Significantly, this is the first experimental study referring to BSF application in the CZTSSe solar cell, which would present a wide range of possibilities for the further development of CZTSSe thin-film solar cells encountering a bottleneck period.

EXPERIMENTAL SECTION

Film Preparation. Back electrode Mo or Mo:Nb was prepared on a soda lime glass (SLG) substrate via direct current (dc) magnetron sputtering at a power of 150 W. Argon (99.999%) was used as the working gas and the deposition temperature was maintained at 500 °C during the whole sputtering process. A small Nb sheet (99.95%, ZhongNuo Advanced Material (Beijing) Technology Co., Ltd.) was placed on the Mo target surface (99.99%, ZhongNuo Advanced Material (Beijing) Technology Co., Ltd.) to achieve Nb-doped Mo films. Then, the sputtered Mo and Mo:Nb films were selenized at 552 °C for 11 min under flowing nitrogen/selenium vapor to obtain $MoSe_2$ and $MoSe_2$:Nb films. The CZTSSe absorber was fabricated by a two-step procedure. First, $Cu(CH_3COO)_2{\cdot}H_2O$ (6.00 mmol, 99.95%, Aladdin), $SnCl_2{\cdot}2H_2O$ (3.75 mmol, 99.99%, Aladdin), $ZnCl_2$ (4.39 mmol, 99.9%, Aladdin), and CH_4N_2S (29.99 mmol, 99%, Aladdin) were dissolved into dimethyl sulfoxide (10 mL, 99.9%, Aladdin), under magnetic stirring for 2 h at room temperature. The Cu/(Zn + Sn) and Zn/Sn are ~0.74 and ~1.17, respectively. A pellucid and light-yellow CZTS precursor solution was obtained. Second, the CZTS precursor solution was spin-coated on SLG/Mo or SLG/Mo:Nb substrates at 800 rpm for 5 s and then 3000 rpm for 30 s. Subsequently, it was roasted at 300 °C for 3 min on the hot plate inside the glove box containing N_2 (99.999%), and this process was repeated 10 times to obtain the CZTS precursor film with desired thickness.

Device Fabrication. CZTSSe solar cells without and with BSF were prepared using a typical structure of SLG/Mo (Mo:Nb)/CZTSSe/CdS/i-ZnO/indium tin oxide (ITO)/Al grid, respectively. The absorber was obtained by post-selenizing the CZTS precursor film mentioned above to facilitate grain coarse utilizing selenium pellets (99.999%, Aladdin) as selenium source in a graphite box under flowing nitrogen (99.999%). The selenization temperature and time were controlled at 552 °C and 15 min, respectively. When the CZTSSe films (~1 μm) cooled down to room temperature, immediately, buffer layer CdS thin films (50 nm) were deposited on the surface of the absorber by chemical bath deposition (CBD). The Cd and S sources were $CdSO_4{\cdot}8/3H_2O$ (99.5%, Aladdin) and CH_4N_2S (99%, Aladdin), respectively. During the CBD process, the temperature and time were maintained at 75 °C for 14 min, and NH_4Cl (99.5%, Aladdin) was used as the buffering agent. Next, window layers of i-ZnO (50 nm) followed rapidly by ITO (260 nm) were deposited on top of the CdS layer using radio frequency magnetron sputtering. No antireflection coating was applied. Finally, the Al grid was thermally evaporated through a shadow mask to arrange the top contact fingers on the surface of the ITO layer, and the active area of each cell is 0.19 cm^2.

Characterization. X-ray diffraction (XRD) measurement was conducted by a DX-2700 X-ray diffractometer with Cu Kα radiation (λ = 1.5406 Å). Raman spectra were recorded via a HoribaJobin Yvon HR800 confocal Raman system with an excitation wavelength of 473 nm. The focused spot size is 1 μm, and the laser power was controlled strictly below 1 mW to eliminate the detrimental effect caused by laser heating. The morphology and composition were characterized by HITACHI S-4800 field-emission scanning electron microscopy (SEM) equipped with an energy-dispersive X-ray spectroscopy (EDX) system (EDAX Genesis 2000). EDX measurements were carried out using a Si-drift detector attached to SUTW-Sapphire at an accelerating voltage of 17 keV. The electrical properties of thin films were studied by van der Pauw configuration in an electrical transport property measurement system (Lake shore 7600 Hall) at room temperature. In order to further confirm the conduction type of the $MoSe_2$ and $MoSe_2$:Nb films, field-effect transistors (FETs) based on an electrolyte gate with $MoSe_2$ and $MoSe_2$:Nb channels were fabricated. The output characterizations of the FETs were carried out. The ionic droplets, $C_{10}H_{20}F_6N_2O_5S_2$, (DEME-TFSI, 99%, Shanghai Aichun Biological Technology Co., Ltd.) were used as the electrolyte gate. The composition and chemical state of the Nb element in the $MoSe_2$:Nb film were verified by X-ray photoelectron spectroscopy (XPS) (ESCALAB MARK II, VG Inc.) using an Al Kα

DOI: 10.1021/acsami.9b08946
ACS Appl. Mater. Interfaces 2019, 11, 31851−31859

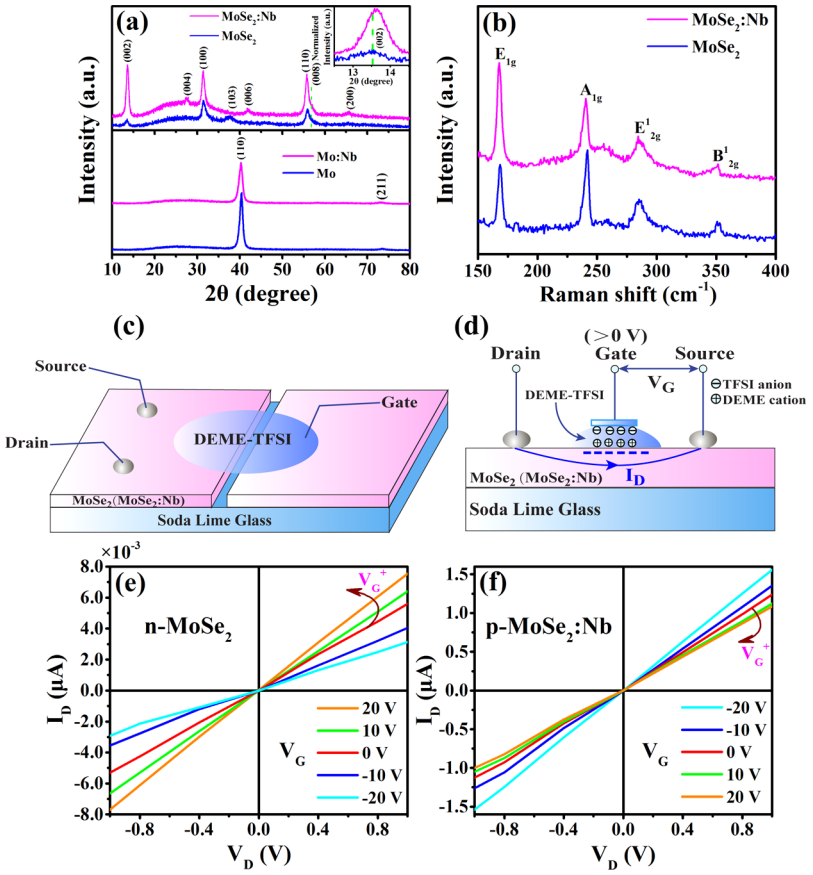

Figure 2. Characterizations of crystal structure and conduction type for the Nb-doped Mo and $MoSe_2$ films. (a) XRD patterns for the Mo, Mo:Nb, $MoSe_2$, and $MoSe_2$:Nb films. To distinguish the diffraction peak shift, the inset shows the enlarged area near the (002) diffraction peaks. (b) Raman spectra of the $MoSe_2$ and $MoSe_2$:Nb films. (c) Top-view and (d) front-view schematic diagrams of the $MoSe_2$-based FETs with a drop of ionic liquid electrolyte (DEME-TFSI) as a gate, covering the $MoSe_2$ (or $MoSe_2$:Nb) channel. The I_D-V_D characteristics of the FETs with (e) n-$MoSe_2$ and (f) p-$MoSe_2$:Nb channels at various V_G.

as X-ray source, with a base pressure of 10^{-8} Pa in the analysis chamber. The ultraviolet photoelectron spectroscopy (UPS) of the sample was carried out via a Thermo ESCALAB 250 surface analysis system with photon energy of 21.22 eV. For the measurements of PV performance, current density−voltage ($J-V$) curves of CZTSSe solar cells were measured using a Keithley 2400 source meter under simulated AM 1.5G solar illumination that has been calibrated to 100 mW·cm^{-2} by a Newport officially certified crystalline Si reference cell. Furthermore, temperature-dependent $J-V$ characteristics were recorded in a closed-cycle helium cryostat system driven by an 8200 Compressor (CTI-CRYOGENICS, U.S.A.), and the sample temperature is measured with a silicon diode. External quantum efficiency (EQE) curves were obtained by a Zolix SCS100 QE system equipped with a 150 W xenon light source, an integrating sphere, and a lock-in amplifier. The EQE signal was amplified and collected via lock-in technique. The capacitance−voltage ($C-V$) data were measured at room temperature by using 20 mV and 100 kHz alternating current excitation source with dc bias from −1.0 to 0.5 V under dark condition.

RESULTS AND DISCUSSION

XRD characterization was utilized to reveal the change in crystal phase of Mo:Nb and $MoSe_2$:Nb thin films where Mo is partially substituted by Nb, and the results are displayed in Figure 2a. It can be seen that the diffraction peaks for the Mo and Mo:Nb films are well-indexed to the cubic phase (JCPDS card no. 42-1120). The (110) peak of the Mo:Nb film reveals a shift toward the lower diffraction angle with respect to the Mo film, indicating a larger lattice constant for the Mo:Nb because of the bigger Nb-substituted Mo atoms (Nb_{Mo}). The XRD patterns of $MoSe_2$ and $MoSe_2$:Nb films exhibit similar peak positions that belong to (002), (004), (100), (103), (006), (110), (008), and (200) diffraction peaks of hexagonal structures (JCPDS card no. 29-0914), respectively. We also calculated the lattice parameters using these XRD data (Table S1, Supporting Information). It is found that the lattice constant along the c-axis is shrunken from 12.934 Å for $MoSe_2$ to 12.922 Å for $MoSe_2$:Nb (inset of Figure 2a), whereas the lattice constant a within the plane varied negligibly (from 3.285 to 3.288 Å). Besides, combining the slight volume shrinkage $\left(\Delta\frac{c}{a} \approx 0.007\right)$, it is concluded that Nb takes a substitutional site (Nb_{Mo}), rather than interstitial doping (Nb_i).[12] Consequently, less electrons engaged in nonbonding orbitals because of Nb_{Mo} replacement, which weakened the repulsion between Se atoms and nonbonding orbitals.[12] Furthermore, the repulsion of Se $3p_z$ orbitals between sheets is weaker compared to that of Se $3p_x$ and Se $3p_y$ orbitals within a sheet. Then, structure rearrangement occurred to balance the repulsion; as a result, a-axis increased and c-axis decreased simultaneously.

To further confirm the presence of $MoSe_2$ or $MoSe_2$:Nb, Raman spectroscopy investigation was conducted, as Raman spectroscopy is a sensitive method to detect TMdCs. As shown in Figure 2b, four Raman modes were observed, which are assigned to E_{1g} (in-plane), A_{1g} (out-of-plane), E^1_{2g} (in-plane),

DOI: 10.1021/acsami.9b08946
ACS Appl. Mater. Interfaces 2019, 11, 31851−31859

Table 1. Electrical Properties Including the Resistivity (ρ), Carrier Concentration (N_{Hall}), Mobility (μ), and Conduction Type of Mo, Mo:Nb, $MoSe_2$, $MoSe_2$:Nb, and CZTSSe Films, Respectively

sample	ρ [Ω·cm]	N_{Hall} [cm^{-3}]	μ [$cm^2\ V^{-1}\ s^{-1}$]	conduction type
Mo	2.50×10^{-4}	4.88×10^{23}	5.11×10^{-2}	p-type
Mo:Nb	2.91×10^{-4}	5.01×10^{23}	4.27×10^{-2}	p-type
$MoSe_2$	6.37×10^{1}	3.09×10^{17}	3.02×10^{-1}	n-type
$MoSe_2$:Nb	1.86×10^{0}	3.54×10^{18}	9.52×10^{-1}	p-type
CZTSSe	6.70×10^{1}	1.33×10^{16}	6.94×10^{0}	p-type

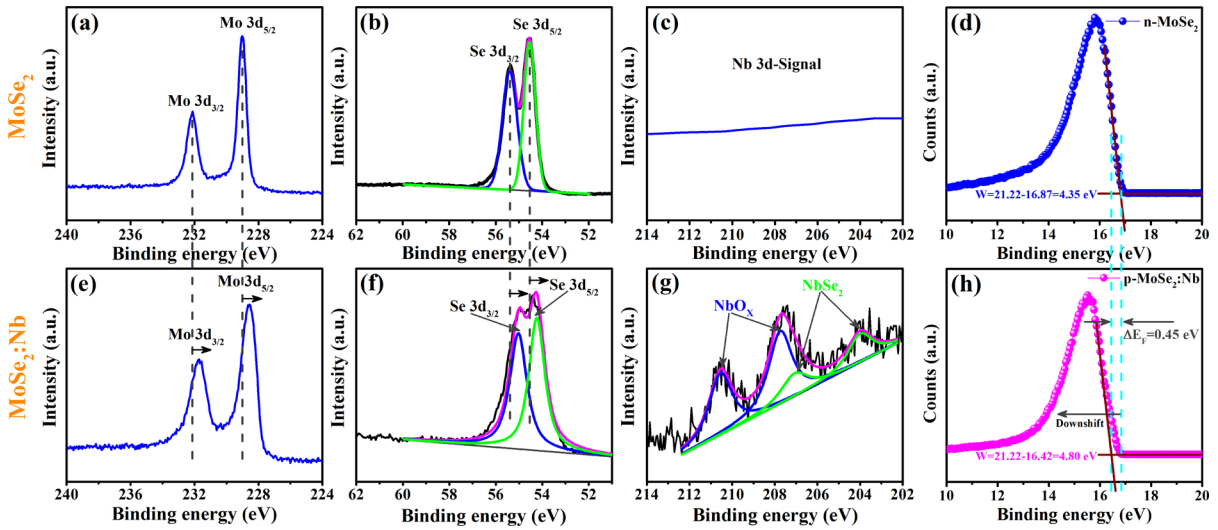

Figure 3. (a,e) Mo 3d, (b,f) Se 3d, and (c,g) Nb 3d XPS spectra as well as (d,h) UPS spectra for the $MoSe_2$ and $MoSe_2$:Nb films, respectively.

and B^1_{2g} of $MoSe_2$.[15] No peaks related to the possible $NbSe_2$ were found, which is consistent with XRD findings. It should be pointed out that a slight red shift of E^1_{2g} ($-0.673\ cm^{-1}$) and A_{1g} ($-1.353\ cm^{-1}$) peaks occurred after being doped by Nb, as listed in Table S2 (Supporting Information). The E^1_{2g} mode is sensitive to the built-in strain, whereas the A_{1g} mode allows us to acquire information on the interlayer van der Waals interactions of TMdCs.[16,17] Furthermore, according to the report of Rice et al.[18] and Conley et al.[19] the E^1_{2g} and A_{1g} modes would be shifted to a lower frequency with increasing lattice strain. Thus, in terms of the variation in the lattice distance between Mo−Se and Nb−Se bonds,[20−22] it is reasonable to illustrate that Nb-doping has led to the increased strain (Table S1, Supporting Information). Therefore, compared to the $MoSe_2$ case, we attribute the red shift of E^1_{2g} and A_{1g} modes of $MoSe_2$:Nb to the effect of strain variation. Interestingly, the decreased vibrational frequency of E^1_{2g} and A_{1g} modes also supported the XRD results that *a*-axis expansion and *c*-axis contraction of the lattice took place as Nb is doped into $MoSe_2$. Therefore, Nb was doped successfully into Mo or $MoSe_2$.

The electrical property of the interfacial $MoSe_2$:Nb layer plays a key role in improving the performance of CZTSSe solar cells because it determines the BSF nature. To determine the electrical properties of the $MoSe_2$ and $MoSe_2$:Mo films, we performed Hall-effect measurements. The results are listed in Table 1. A transition from n- to p-type conduction was realized as Nb was doped into $MoSe_2$. Also, the p-$MoSe_2$:Nb exhibits a dramatic decrease in resistivity (ρ) (from 63.7 to 1.86 Ω·cm) and the increase in carrier concentration (N_{Hall}) in comparison with that of the n-$MoSe_2$ film, which leads to favorable impacts on the device performance. To further validate the transition in conduction type of $MoSe_2$:Nb, we fabricated FETs with $MoSe_2$ and $MoSe_2$:Nb channels. The schematic diagrams of the FETs' structure are shown in Figure 2c,d. The gate bias (V_G)-dependent plots of drain current (I_D) versus drain voltage (V_D) (output characterization) for the FETs with $MoSe_2$ and $MoSe_2$:Nb channels were recorded, as shown in Figure 2e,f. For the FET with the $MoSe_2$ channel, the I_D at a certain positive V_D increases with increasing positive V_G (V_G^+), suggesting an intrinsic n-type behavior of the $MoSe_2$.[23] In contrast, for the FET with the $MoSe_2$:Nb channel, the I_D exhibits a different trend, which decreases with a V_G^+ increment. Such variation further confirms the p-type conduction of the $MoSe_2$:Nb film. Note that similar variations were observed as V_G transformed to a negative value in consideration of the fact that negative V_G injects hole, which further confirms the discussions above. It should be emphasized that the accuracy of Hall-effect and FETs results is dependent on the sole phase $MoSe_2$ or $MoSe_2$:Nb, that is, absence of the Mo or Mo:Nb phase because of their tremendous difference in resistivity (Table 1). From Figure 2a (upper-half), the other characteristic peaks derived from Mo, Mo:Nb and possible floating Se powders on the surface of $MoSe_2$ or $MoSe_2$:Nb films were not detected. This result suggests that two samples have been fully selenized, supporting their conduction type determination from Hall-effect and FET measurements. Besides, it is also found that p-$MoSe_2$:Nb exhibits remarkably nearly 300-fold improvement in N_{Hall} compared to that of the p-CZTSSe film (Table 1). As a result, a p-$MoSe_2$:Nb/p-CZTSSe heterojunction BEI with self-organized BSF was formed in the CZTSSe solar cell through an indispensable selenization process, being advantageous for the reduction of carrier recombination at the BEI (discussed later).[8,9]

DOI: 10.1021/acsami.9b08946
ACS Appl. Mater. Interfaces 2019, 11, 31851−31859

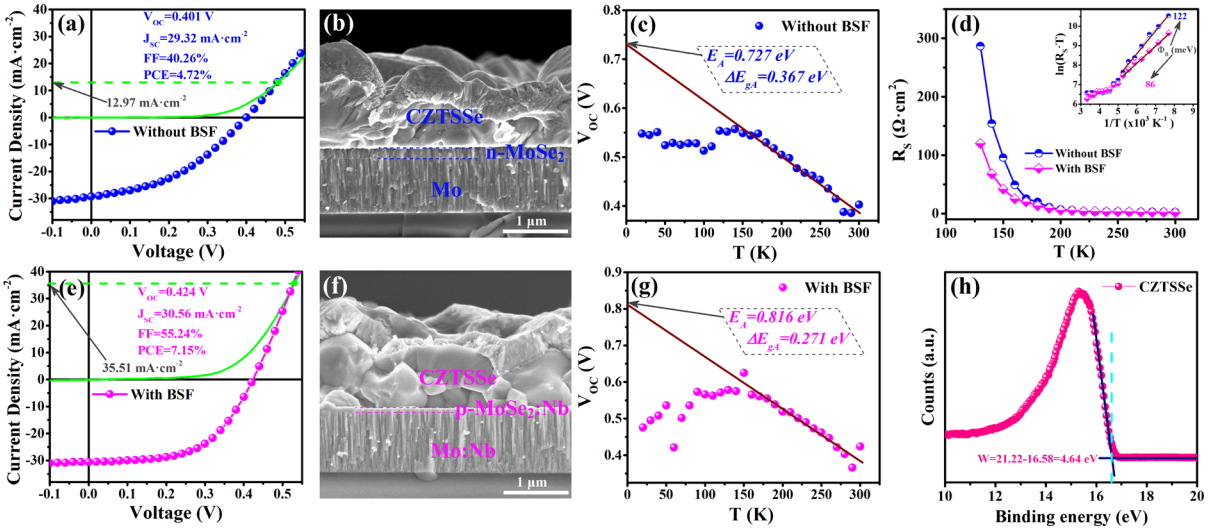

Figure 4. PV performance characterizations and cross-sectional morphologies for the CZTSSe solar cells (a–c) without and (e–g) with BSF, respectively. (a,e) J–V curves under AM 1.5G illumination. (b,f) Cross-sectional SEM images. (c,d,g) Temperature-dependence of V_{OC} and R_S; the inset shows that the back barrier height Φ_B is extracted by $\ln(R_S \cdot T^2)$ vs $1000/T$. (h) UPS spectra of the CZTSSe film.

The Nb dopant in the $MoSe_2$:Nb film was further analyzed using XPS and UPS measurements, as shown in Figure 3. The binding energies of Mo 3d and Se 3d in $MoSe_2$:Nb are downshifted by −0.42 eV compared to those of $MoSe_2$, which is a distinct evidence for the incorporation of Nb into the $MoSe_2$:Nb film.[24,25] Moreover, according to the viewpoint of previous studies,[25,26] this binding energy difference indicates that the Fermi level has shifted toward lower energy after Nb-doping, being beneficial for its p-type transition. Also, UPS spectra revealed the p-type doping effect in $MoSe_2$:Nb, as seen in Figure 3d,h, and the Fermi level of p-$MoSe_2$:Nb is 0.45 eV smaller than that of n-$MoSe_2$, which is in good agreement with the binding energy variation of Mo 3d and Se 3d. No Nb-related peak was observed for the $MoSe_2$ film, as shown in Figure 3c. In contrast, the Nb 3d peak (Nb $3d_{5/2}$)[27] assigned to Nb atoms incorporated within the $MoSe_2$ lattice is observed clearly in $MoSe_2$:Nb (Figure 3g). Additionally, it is also found that the other two higher binding energy components correspond to native oxide-related (NbO_x).[28] Similar phenomena were reported by Jin et al.[24] and Deepak et al.,[25] and they hold a point that the oxidized Nb appears to form a sub-nanometer coating (NbO_x) on the surface of the film. Besides, the elemental composition was evaluated from XPS and EDX measurements (Table S3, Supporting Information). By comparison, the Nb content in XPS data is more accurate because of its superior element stoichiometric ratio.

Figure 4a,e illustrates the J–V curves of the CZTSSe solar cells without and with BSF, respectively. The corresponding device and electric parameters were collected and are listed in Tables 2 and 3, respectively. We found a remarkable increase of PCE from 4.72 to 7.15% after introducing BSF. The improvement mechanism of PCE is elucidated in detail below.

Table 2. PV Parameters of CZTSSe Solar Cells with Various BEI Structures

BEI	V_{OC} [V]	J_{SC} [mA·cm^{-2}]	FF [%]	PCE [%]
SLG/Mo/n-$MoSe_2$	0.401	29.32	40.26	4.72
SLG/Mo:Nb/p-$MoSe_2$:Nb	0.424	30.56	55.24	7.15

Table 3. Electric Parameters of CZTSSe Solar Cells with Different BEI Structures

BEI	R_S [Ω·cm^2]	R_{Sh} [Ω·cm^2]	A	J_0 [mA·cm^{-2}]
SLG/Mo/n-$MoSe_2$	4.39	82.11	2.38	3.58×10^{-2}
SLG/Mo:Nb/p-$MoSe_2$:Nb	1.75	497.51	2.09	1.26×10^{-2}

It is commonly known that n-$MoSe_2$ or n-MoS_2 is formed at the BEI during indispensable selenization or sulfurization processes, and they affect V_{OC} and band alignment at the BEI, exerting deleterious effects on the device performance.[29,30] Moreover, according to the report of Biccari et al.[31] that n-MoS_2 causes a barrier at the MoS_2/CZTS interface, it has been suggested to have p-MoS_2 for the sake of achieving better results. In this work, the desirable p-$MoSe_2$:Nb/p-CZTSSe interface was produced instead of the conventional n-$MoSe_2$/p-CZTSSe interface, that is, BSF was formed at the BEI. Therefore, the improved PCE can be attributed to the contribution of the V_{OC} improvement from 0.401 to 0.424 V and the dramatic boost of FF from 40.26 to 55.24%, primarily stemming from the doubling aspects of increased shunt resistance (R_{Sh}), decreased series resistance (R_S), and alleviative recombination velocity of BEI induced by BSF.[32,33] It should be noted that the rise of R_{Sh} is reasonably because of the reduced electric leakage as a result of the BSF generated locally passivated to the back electrode.[33,34] Also, ultrathin NbO_x (sub-nanometer level)[24,25] was coated on the surface of the SLG/Mo:Nb substrate. Therefore, one has to consider the reduced secondary phases at the BEI induced by the blocking effect of the NbO_x layer for the reaction between the absorber and the back electrode, which is partly responsible for the higher R_{Sh}. Furthermore, the growth of the interfacial $MoSe_2$:Nb layer formed during the selenization process was also suppressed by the blocking effect mentioned above. The result is a decrease in the thickness of the interfacial $MoSe_2$:Nb layer (Figure 4b,f) and thus smaller R_S accordingly (Table 3), further considering that p-$MoSe_2$:Nb has lower ρ in comparison with that of n-$MoSe_2$ (Table 1). The other noteworthy finding is that the smaller R_S is also ascribed to the decreased back contact barrier height arising from the BSF.[8,9]

DOI: 10.1021/acsami.9b08946
ACS Appl. Mater. Interfaces 2019, 11, 31851–31859

It has been accepted that the cross-over point defined as the non-superposition behavior between the light and dark $J-V$ curve is indicative of the presence of a back contact barrier,[35,36] that is, contact resistance of the back electrode that is one of the sources to R_S. From Figure 4a,e, the matching current density of the cross-over point has achieved an appreciable enhancement (from 12.97 to 35.51 mA·cm^{-2}) with the formation of BSF, suggesting a lower barrier height and thus smaller R_S. To verify the reliability of $J-V$ data, the statistics of device parameters including V_{OC}, J_{SC}, FF, and PCE were obtained based on 18 devices, as shown in Figure 5. According

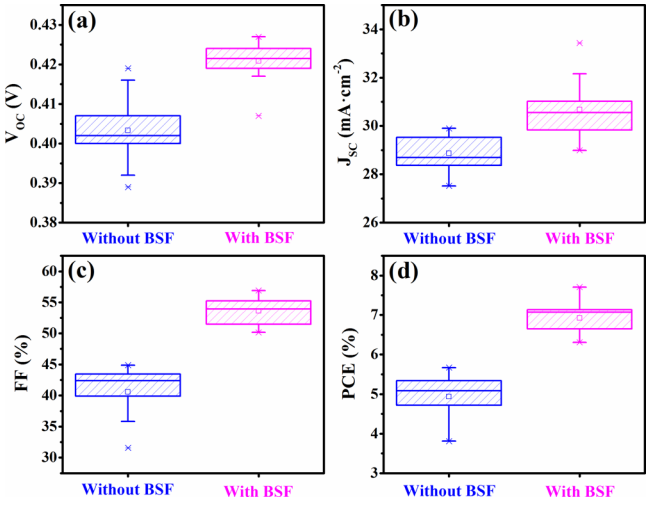

Figure 5. Device parameter statistics of the CZTSSe cells without and with BSF, (a) V_{OC}, (b) J_{SC}, (c) FF, and (d) PCE, respectively. The sample size in each column is 18 devices.

to the statistical data, a relationship can be observed between the device performance and BSF application. After introducing BSF, V_{OC} and J_{SC} improved to some extent, especially FF witnessed an appreciable rising from ∼40.55 to ∼53.62%. Then, the average PCE was increased from ∼4.94 to ∼6.95%.

To gain a better understanding on the diminished interface recombination, temperature (T) dependence of $J-V$ measurement was adopted. Figure 4c,g plots the temperature dependence of V_{OC} for the device without and with BSF, respectively. As is known to all, the relationship between V_{OC} and T can be expressed as eq 1[37−39]

$$V_{OC} = \frac{E_A}{q} - \frac{AkT}{q}\ln\frac{J_{00}}{J_L} \quad (1)$$

where E_A, q, k, J_{00}, and J_L represent activation energy for recombination, electron charge, Boltzmann constant, reverse saturation current prefactor, and photocurrent density, respectively. According to the report of Wang et al.[40] that V_{OC} versus T should be a linear relation based on eq 1, extrapolation of which yields E_A value at 0 K assuming ideal factor (A), J_{00} and J_L are not strongly temperature-dependent. In our results (Figure S1, Supporting Information), the variation of these parameters with T (300−200 K) follows the regularity mentioned above; then, E_A can be estimated to some degree. It can be seen from Figure 4c,g that the extracted E_A of two cells are distinctly lower than their E_g (E_g was calculated by EQE shown in Figure 6b), which is a good indicator of dominating interface recombination.[2,41−44] Notably, when BSF is applied, the E_A is closer to the corresponding E_g, that is, smaller ΔE_{gA}, implying a reduced interface recombination. An identical conclusion was evidenced by the smaller A and reversion saturation current density (J_0) for the device with BSF (Table 3). In addition, according to the study of Gunawan et al.,[38] the R_S of the solar cell can be denoted as eq 2 below

$$R_S = R_0 + \frac{k}{qA^*T}\exp\left(\frac{\Phi_B}{kT}\right) \quad (2)$$

where k, A^*, and Φ_B are the Boltzmann constant, effective Richardson constant, and back contact barrier height, respectively. It should be noted that R_0 is the background series resistance rooting in different factors (e.g., contact grid and distributed resistance of the window layer). Particularly, it is nearly independent of the low temperatures and only contributing at the temperatures above 300 K. In other words, R_0 can be regarded as a negligible factor for R_S at a lower temperature. Figure 4d depicts the temperature-dependent R_S for CZTSSe cells without and with BSF, respectively. R_S increases with decreasing temperature, especially at a lower temperature. To estimate Φ_B, $\ln(R_S \cdot T)$ versus $1/T$ was replotted, as shown in the Figure 4d inset. It is seen that the data exhibit linearity well at a high $1/T$ stage, the slope yields Φ_B of 122 and 86 meV for the device without and with BSF, respectively. This result suggests that BSF exerts an appreciable impact in lowering down the Φ_B of the CZTSSe cell, coinciding with its lower R_S and higher cross-over point (Figure 4a,e). This positive effect of BSF in Φ_B reduction can be elucidated by the band alignment between $MoSe_2$

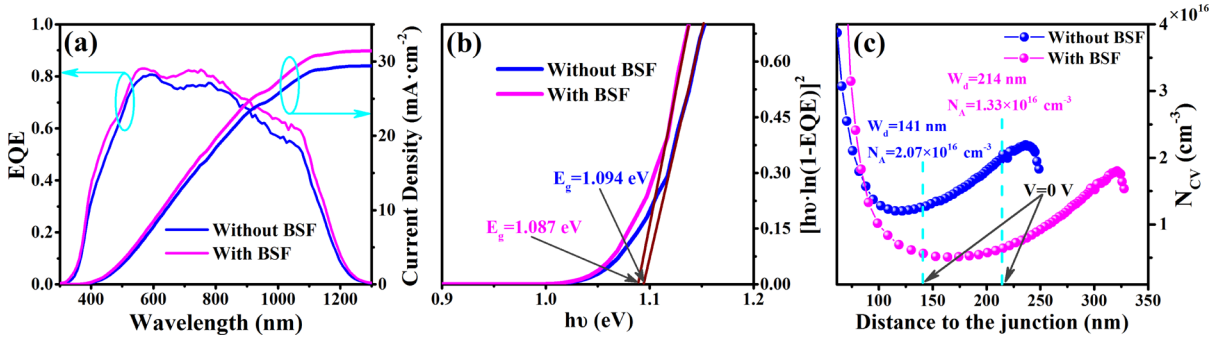

Figure 6. Performance characterizations of the CZTSSe solar cells without and with BSF. (a) EQE and the corresponding integrated current from EQE spectra. (b) Determination of E_g of the absorber based on EQE spectra. (c) $C-V$ curves, respectively.

DOI: 10.1021/acsami.9b08946
ACS Appl. Mater. Interfaces 2019, 11, 31851−31859

($MoSe_2$:Nb) and CZTSSe. Figure 4h shows the UPS spectrum of the CZTSSe film, which extracts a work function of 4.64 eV that is situated between the corresponding values of $MoSe_2$ and $MoSe_2$:Nb (Figure 3d,h). Therefore, with the incorporation of BSF, it is favorable to accelerate the photo-generated hole transportation from the absorber to the back electrode; thereby, Φ_B decreased, as displayed in Figure 1.

In order to deeply investigate device performance improvement, EQE was measured for CZTSSe solar cells without and with BSF, as shown in Figure 6a. Obviously, the EQE was improved in the whole visible region via introducing BSF, which might be explained by the considerably reduced R_S (Table 3) that has been analyzed in the $J-V$ section. Also, in terms of the BSF effect, the more effective charge carrier collection in the deep region of the CZTSSe film is in favor of the higher EQE.[45] Given that the photo-induced carrier to incident photon quantity ratio represents EQE, we can estimate the J_{SC} on the basis of eq 3

$$J_{SC} = q\int_0^\infty F_{1.5}(\lambda)\cdot \mathrm{EQE}(\lambda)\cdot \mathrm{d}\lambda \tag{3}$$

where q and $F_{1.5}(\lambda)$ are electron charge and the incident photons density under AM 1.5G solar illumination, respectively. In Figure 6a, we derived the current density of 29.42 and 31.13 $mA\cdot cm^{-2}$ by integrating the EQE spectra of CZTSSe cells without and with BSF, respectively, further validating our experimental J_{SC} values (Figure 4a,e). Additionally, E_g of the absorber was evaluated from the EQE data plotted as $[h\upsilon\cdot\ln(1 - \mathrm{EQE})]^2$ versus $h\upsilon$, where the $h\upsilon$ is photo energy, as illustrated in Figure 6b. It has been found that E_g of the CZTSSe film has no clear correlation with BSF introduction, and they are in the range of 1.087−1.094 eV. EQE improvement in the long-wavelength region also mirrors the superior separation ability or collection efficiency of photo-induced carriers. Therefore, we further performed $C-V$ characterization on the device without and with BSF, as displayed in Figure 6c. The carrier density (N_{C-V}) of the CZTSSe film for the cell without BSF is calculated as 2.07×10^{16} cm^{-3}, and its width of depletion region (W_d) is estimated to be 141 nm by eq 4

$$W_d = \frac{\xi_0\xi_r A_{cell}}{C} \tag{4}$$

where A_{cell} is the area of the solar cell, ξ_0 and ξ_r denote the free space permittivity (commonly $\sim 8.85 \times 10^{-12}$ $F\cdot m^{-1}$) and the relative dielectric constant of the absorber, respectively. By using the method reported by Persson,[46] here, ξ_r values have been taken to be 8.13 and 8.19 for CZTSSe cells without and with BSF, respectively. After introducing BSF, N_{C-V} decreased to 1.33×10^{16} cm^{-3}, which is possibly because of the blocking effect for Na diffusion from SLG induced by the NbO_x layer at the BEI. As a result, the W_d has enlarged to 214 nm accordingly. It is generally established that the absorption coefficient gets smaller as the light wavelength increases. Indeed, much long-wavelength incident light was absorbed in the bottom of the absorber film, then, photon-induced carrier of which cannot be collected effectively if the depletion region is narrow.[45] Consequently, the higher EQE response of the device with BSF at the long wavelength region should be attributed not only to the decreased R_S but also to the increased W_d.

CONCLUSIONS

In summary, we have reported the reduction of carrier recombination at the BEI by introducing BSF. The self-organized BSF was realized by the conduction type transition from n- to p-type via Nb-doping for the interfacial $MoSe_2$ layer. The transition was validated by Hall-effect measurements and output characterizations of FETs. The PCE of the device with the BSF increased dramatically from 4.72 to 7.15%, which is explained by the increased V_{OC} (from 0.401 to 0.424 V) and FF (from 40.26 to 55.24%). The higher V_{OC} and FF are attributed to the doubling aspects of increased R_{Sh} (from 82.11 to 497.51 $\Omega\cdot cm^2$), decreased R_S (from 4.39 to 1.75 $\Omega\cdot cm^2$), and alleviative recombination velocity of BEI induced by the BSF effect. The rise of R_{Sh} is reasonably ascribed to the reduced electric leakage as a result of the BSF generated locally passivated for the back electrode. A decrease in the thickness of the p-$MoSe_2$:Nb layer is in favor of the smaller R_S accordingly. Also, p-$MoSe_2$:Nb has a much lower ρ than that of n-$MoSe_2$, contributing to the decrease of R_S. The reduced interface recombination after incorporation of BSF was proved by the smaller A, J_0, and ΔE_{gA}. EQE and $C-V$ results manifested the superior separation ability of photo-induced carriers for the device with BSF.

ASSOCIATED CONTENT

Supporting Information

The Supporting Information is available free of charge on the ACS Publications website at DOI: 10.1021/acsami.9b08946.

Lattice parameters, frequency vibration of Raman modes, and elemental composition for $MoSe_2$, $MoSe_2$:Nb films; and temperature dependence data of the ideal factor (A), reverse saturation current prefactor (J_{00}), and photocurrent density (J_L), respectively (PDF)

AUTHOR INFORMATION

Corresponding Authors

*E-mail: binyao@jlu.edu.cn (B.Y.).
*E-mail: liyongfeng@jlu.edu.cn (Y.L.).

ORCID

Bin Yao: 0000-0003-0748-3220
Yongfeng Li: 0000-0002-9725-0692

Author Contributions

All authors have given approval to the final version of the paper.

Notes

The authors declare no competing financial interest.

ACKNOWLEDGMENTS

This work is supported by the National Natural Science Foundation of China under Grant Nos. 61774075, The Science and Technology Development Project of Jilin Province under grant No. 20170101142JC, and Natural Science Foundation of Jilin Province under grant No. 20180101227JC. This work was also supported by High Performance Computing Center of Jilin University, China.

REFERENCES

(1) Kim, J.; Hiroi, H.; Todorov, T. K.; Gunawan, O.; Kuwahara, M.; Gokmen, T.; Nair, D.; Hopstaken, M.; Shin, B.; Lee, Y. S.; Wang, W.; Sugimoto, H.; Mitzi, D. B. High Efficiency $Cu_2ZnSn(S,Se)_4$ Solar

DOI: 10.1021/acsami.9b08946
ACS Appl. Mater. Interfaces 2019, 11, 31851−31859

Cells by Applying a Double In_2S_3/CdS Emitter. *Adv. Mater.* **2014**, *26*, 7427−7431.
(2) Mitzi, D. B.; Gunawan, O.; Todorov, T. K.; Wang, K.; Guha, S. The Path towards a High-Performance Solution-Processed Kesterite Solar Cell. *Sol. Energy Mater. Sol. Cells* **2011**, *95*, 1421−1436.
(3) Mitzi, D. B.; Gunawan, O.; Todorov, T. K.; Barkhouse, D. A. R. Prospects and Performance Limitations for Cu-Zn-Sn-S-Se Photovoltaic Technology. *Philos. Trans. R. Soc., A* **2013**, *371*, 20110432.
(4) Teinhagen, C. S.; Panthani, M. G.; Akhavan, V.; Goodfellow, B.; Koo, B.; Korgel, B. A. Synthesis of Cu_2ZnSnS_4 Nanocrystals for Use in Low-Cost Photovoltaics. *J. Am. Chem. Soc.* **2009**, *131*, 12554−12555.
(5) Wang, W.; Winkler, M. T.; Gunawan, O.; Gokmen, T.; Todorov, T. K.; Zhu, Y.; Mitzi, D. B. Device Characteristics of CZTSSe Thin-Film Solar Cells with 12.6% Efficiency. *Adv. Energy Mater.* **2014**, *4*, 1301465.
(6) Hages, C. J.; Levcenco, S.; Miskin, C. K.; Alsmeier, J. H.; Abou-Ras, D.; Wilks, R. G.; Bär, M.; Unold, T.; Agrawal, R. Improved Performance of Ge-Alloyed CZTGeSSe Thin-Film Solar Cells Through Control of Elemental Losses. *Prog. Photovolt. Res. Appl.* **2015**, *23*, 376−384.
(7) Kaur, K.; Kumar, N.; Kumar, M. Strategic Review of Interface Carrier Recombination in Earth Abundant Cu-Zn-Sn-S-Se Solar Cells: Current Challenges and Future Prospects. *J. Mater. Chem. A* **2017**, *5*, 3069−3090.
(8) Hossain, M. D. S.; Amin, N.; Razykov, T. Prospects of Back Contacts with Back Surface Fields in High Efficiency $Zn_xCd_{1-x}S$/CdTe Solar Cells from Numerical Modeling. *Chalcogenide Lett.* **2011**, *8*, 187−198.
(9) Khosroabadi, S.; Keshmiri, S. H. Design of a High Efficiency Ultrathin CdS/CdTe Solar Cell Using Back Surface Field and Backside Distributed Bragg Reflector. *Opt. Express* **2014**, *22*, A921−A929.
(10) Omrani, M. K.; Minbashi, M.; Memarian, N.; Kim, D.-H. Improve the Performance of CZTSSe Solar Cells by Applying a SnS BSF Layer. *Solid-State Electron.* **2018**, *141*, 50−57.
(11) Khattak, Y. H.; Baig, F.; Toura, H.; Ullah, S.; Marí, B.; Beg, S.; Ullah, H. Effect of CZTSe BSF and Minority Carrier Life Time on the Efficiency Enhancement of CZTS Kesterite Solar Cell. *Curr. Appl. Phys.* **2018**, *18*, 633−641.
(12) Bougouma, M.; Guel, B.; Segato, T.; Legma, J. B.; Ogletree, M. P. D. The Structure of Niobium-Doped $MoSe_2$ and WSe_2. *Bull. Chem. Soc. Ethiop.* **2008**, *22*, 225−236.
(13) Dolui, K.; Rungger, I.; Pemmaraju, C. D.; Sanvito, S. Possible Doping Strategies for MoS_2 Monolayers: An ab Initio Study. *Phys. Rev. B: Condens. Matter Mater. Phys.* **2013**, *88*, 075420.
(14) Legma, J. B.; Vacquier, G.; Traoré, H.; Casalot, A. Improvement in Photocurrent with n-Type Niobium- and Rhenium-Doped Molybdenum and Tungsten Diselenide Single Crystals. *Mater. Sci. Eng., B* **1991**, *8*, 167−174.
(15) Tonndorf, P.; Schmidt, R.; Böttger, P.; Zhang, X.; Börner, J.; Liebig, A.; Albrecht, M.; Kloc, C.; Gordan, O.; Zahn, D. R. T.; de Vasconcellos, S. M.; Bratschitsch, R. Photoluminescence Emission and Raman Response of Monolayer MoS_2, $MoSe_2$, and WSe_2. *Opt. Express* **2013**, *21*, 4908−4916.
(16) Li, Y.; Cain, J. D.; Hanson, E. D.; Murthy, A. A.; Hao, S.; Shi, F.; Li, Q.; Wolverton, C.; Chen, X.; Dravid, V. P. Au@MoS_2 Core-Shell Heterostructures with Strong Light-Matter Interactions. *Nano Lett.* **2016**, *16*, 7696−7702.
(17) Zhou, K.-G.; Withers, F.; Cao, Y.; Hu, S.; Yu, G.; Casiraghi, C. Raman Modes of MoS_2 Used as Fingerprint of Van Der Waals Interactions in 2-D Crystal-Based Heterostructures. *ACS Nano* **2014**, *8*, 9914−9924.
(18) Rice, C.; Young, R. J.; Zan, R.; Bangert, U.; Wolverson, D.; Georgiou, T.; Novoselov, K. S. Raman-Scattering Measurements and First-Principles Calculations of Strain-Induced Phonon Shifts in Monolayer MoS_2. *Phys. Rev. B: Condens. Matter Mater. Phys.* **2013**, *87*, 081307.
(19) Conley, H. J.; Wang, B.; Ziegler, J. I.; Haglund, R. F.; Pantelides, S. T.; Bolotin, K. I. Band Gap Engineering of Strained Monolayer and Bilayer MoS_2. *Nano Lett.* **2013**, *13*, 3626−3630.
(20) Choi, S. Y.; Kim, Y.; Chung, H.-S.; Kim, A. R.; Kwon, J.-D.; Park, J.; Kim, Y. L.; Kwon, S.-H.; Hahm, M. G.; Cho, B. Effect of Nb Doping on Chemical Sensing Performance of Two-Dimensional Layered $MoSe_2$. *ACS Appl. Mater. Interfaces* **2017**, *9*, 3817−3823.
(21) Kim, A. R.; Kim, Y.; Nam, J.; Chung, H.-S.; Kim, D. J.; Kwon, J.-D.; Park, S. W.; Park, J.; Choi, S. Y.; Lee, B. H.; Park, J. H.; Lee, K. H.; Kim, D.-H.; Choi, S. M.; Ajayan, P. M.; Hahm, M. G.; Cho, B. Alloyed 2D Metal-Semiconductor Atomic Layer Junctions. *Nano Lett.* **2016**, *16*, 1890−1895.
(22) Yu, Z.; Pan, Y.; Shen, Y.; Wang, Z.; Ong, Z. Y.; Xu, T.; Xin, R.; Pan, L.; Wang, B.; Sun, L.; Wang, J.; Zhang, G.; Zhang, Y. W.; Shi, Y.; Wang, X. Towards Intrinsic Charge Transport in Monolayer Molybdenum Disulfide by Defect and Interface Engineering. *Nat. Commun.* **2014**, *5*, 5290.
(23) Fang, H.; Chuang, S.; Chang, T. C.; Takei, K.; Takahashi, T.; Javey, A. High-Performance Single Layered WSe_2 p-FETs with Chemically Doped Contacts. *Nano Lett.* **2012**, *12*, 3788−3792.
(24) Jin, Y.; Keum, D. H.; An, S.-J.; Kim, J.; Lee, H. S.; Lee, Y. H. A Van Der Waals Homojunction: Ideal p-n Diode Behavior in $MoSe_2$. *Adv. Mater.* **2015**, *27*, 5534−5540.
(25) Deepak, F. L.; Cohen, H.; Cohen, S.; Feldman, Y.; Popovitz-Biro, R.; Azulay, D.; Millo, O.; Tenne, R. Fullerene-Like (IF) $Nb_xMo_{1-x}S_2$ Nanoparticles. *J. Am. Chem. Soc.* **2007**, *129*, 12549−12562.
(26) McDonnell, S.; Addou, R.; Buie, C.; Wallace, R. M.; Hinkle, C. L. Defect-Dominated doping and Contact Resistance in MoS_2. *ACS Nano* **2014**, *8*, 2880−2888.
(27) Cardona, M. Photoemission in Solids II: Case Studies. *Topics in Applied Physics*; Springer Verlag: Berlin/Heidelberg, 1979.
(28) Okazaki, Y.; Tateishi, T.; Ito, Y. Corrosion Resistance of Implant Alloys in Pseudo Physiological Solution and Role of Alloying Elements in Passive Films. *Mater. Trans. JIM* **1997**, *38*, 78−84.
(29) Kato, T.; Hiroi, H.; Sakai, N.; Muraoka, S.; Sugimoto, H. *Proceedings of the 27th European Photovoltaic Solar Energy Conference and Exhibition; EU-PVSEC*: Frankfurt, 2012.
(30) Nishiwaki, S.; Kohara, N.; Negami, T.; Wada, T. $MoSe_2$ Layer Formation at Cu(In,Ga)Se_2/Mo Interfaces in High Efficiency $Cu(In_{1-x}Ga_x)Se_2$ Solar Cells. *Jpn. J. Appl. Phys.* **1998**, *37*, L71.
(31) Biccari, F.; Chierchia, R.; Valentini, M.; Mangiapane, P.; Salza, E.; Malerba, C.; Ricardo, C. L. A.; Mannarino, L.; Scardi, P.; Mittiga, A. Fabrication of Cu_2ZnSnS_4 Solar Cells by Sulfurization of Evaporated Precursors. *Energy Procedia* **2011**, *10*, 187−191.
(32) Singh, K. J.; Sarkar, S. K. Highly Efficient ARC Less InGaP/GaAs DJ Solar Cell Numerical Modeling Using Optimized InAlGaP BSF Layers. *Opt. Quantum Electron.* **2012**, *43*, 1−21.
(33) Godlewski, M. P.; Baraona, C. R.; Brandhorst, H. W., Jr Low-High Junction Theory Applied to Solar Cells. *Solar Cells* **1990**, *29*, 131−150.
(34) Mandelkorn, J.; Lamneck, J. H., Jr. A New Electric Field Effect in Silicon Solar Cells. *J. Appl. Phys.* **1973**, *44*, 4785−4787.
(35) Niemegeers, A.; Burgelman, M. Effects of the Au/CdTe Back Contact on IV and CV Characteristics of Au/CdTe/CdS/TCO Solar Cells. *J. Appl. Phys.* **1997**, *81*, 2881−2886.
(36) Liu, F.; Sun, K.; Li, W.; Yan, C.; Cui, H.; Jiang, L.; Hao, X.; Green, M. A. Enhancing the Cu_2ZnSnS_4 Solar Cell Efficiency by Back Contact Modification: Inserting a Thin TiB_2 Intermediate Layer at Cu_2ZnSnS_4/Mo Interface. *Appl. Phys. Lett.* **2014**, *104*, 051105.
(37) Hegedus, S. S.; Shafarman, W. N. Thin-Film Solar Cells: Device Measurements and Analysis. *Prog. Photovolt. Res. Appl.* **2004**, *12*, 155−176.
(38) Gunawan, O.; Todorov, T. K.; Mitzi, D. B. Loss Mechanisms in Hydrazine-Processed $Cu_2ZnSn(Se,S)_4$ Solar Cells. *Appl. Phys. Lett.* **2010**, *97*, 233506.
(39) Nadenau, V.; Rau, U.; Jasenek, A.; Schock, H. W. Electronic Properties of $CuGaSe_2$-Based Heterojunction Solar Cells (Part I. Transport Analysis). *J. Appl. Phys.* **2000**, *87*, 584−593.

DOI: 10.1021/acsami.9b08946
ACS Appl. Mater. Interfaces 2019, 11, 31851−31859

(40) Wang, K.; Gunawan, O.; Todorov, T.; Shin, B.; Chey, S. J.; Bojarczuk, N. A.; Mitzi, D.; Guha, S. Thermally Evaporated Cu_2ZnSnS_4 Solar Cells. *Appl. Phys. Lett.* **2010**, *97*, 143508.
(41) Turcu, M.; Pakma, O.; Rau, U. Interdependence of Absorber Composition and Recombination Mechanism in $Cu(In,Ga)(Se,S)_2$ Heterojunction Solar Cells. *Appl. Phys. Lett.* **2002**, *80*, 2598−2600.
(42) Scheer, R. Activation Energy of Heterojunction Diode Currents in the Limit of Interface Recombination. *J. Appl. Phys.* **2009**, *105*, 104505.
(43) Yan, C.; Huang, J. L.; Sun, K. W.; Johnston, S.; Zhang, Y. F.; Sun, H.; Pu, A. B.; He, M. R.; Liu, F. Y.; Eder, K.; Yang, L. M.; Cairney, J. M.; Ekins-Daukes, N. J.; Hameiri, Z.; Stride, J. A.; Chen, S. Y.; Green, M. A.; Hao, X. J. Cu_2ZnSnS_4 Solar Cells with Over 10% Power Conversion Efficiency Enabled by Heterojunction Heat Treatment. *Nat. Energy* **2018**, *3*, 764−772.
(44) Todorov, T. K.; Tang, J.; Bag, S.; Gunawan, O.; Gokmen, T.; Zhu, Y.; Mitzi, D. B. Beyond 11% Efficiency: Characteristics of State-of-the-art $Cu_2ZnSn(S,Se)_4$ Solar Cells. *Adv. Energy Mater.* **2013**, *3*, 34−38.
(45) Gao, S.; Zhang, Y.; Ao, J.; Li, X.; Qiao, S.; Wang, Y.; Lin, S.; Zhang, Z.; Wang, D.; Zhou, Z.; Sun, G.; Wang, S.; Sun, Y. Insight into the Role of Post-Annealing in Air for High Efficient $Cu_2ZnSn(S,Se)_4$ Solar Cells. *Sol. Energy Mater. Sol. Cells* **2018**, *182*, 228−236.
(46) Persson, C. Electronic and Optical Properties of Cu_2ZnSnS_4 and $Cu_2ZnSnSe_4$. *J. Appl. Phys.* **2010**, *107*, 053710.

DOI: 10.1021/acsami.9b08946
ACS Appl. Mater. Interfaces 2019, 11, 31851−31859